Analysis of C-band spaceborne scatterometers thermal noise

Anis Elyouncha and Xavier Neyt

ABSTRACT

A scatterometer is a radar designed to measure the backscattering coefficient of distributed targets. In order to compute the backscatter from the received power, the scatterometer measures also the thermal noise power. This noise signal is composed of two components, the receiver thermal noise and the viewed ground radiance. The first component is instrument dependent and hence independent of the target and viewing geometry. The second component is target and viewing geometry dependent, it is proportional to the ground target brightness temperature. In this paper the noise signal measured by C-band scatterometers on-board ERS-2 and Metop-A satellites is analyzed. It was found that the noise signal carries valuable geophysical information, which is worth to be exploited. It is shown that the noise signal varies spatially, temporally and with viewing geometry. Thus, different targets (ocean, sea ice, land) could be easily identified. A comparison was carried out between the scatterometer noise and AMSR-E radiometer brightness temperature and high correlation was found. The noise signal processing (mainly noise subtraction) is discussed, including the assessment of the Noise Equivalent Sigma Zero and the Signal-to-noise ratio. This analysis leads to a better understanding of the noise signal and its impact on the backscatter processing.

1. INTRODUCTION

The scatterometer is a real aperture radar designed to measure the backscattering coefficient of distributed targets. The backscattering coefficient or the backscatter is also called sigma naught and is referred to as σ_0. The measurement radiometric accuracy is one of the main concerns in the scatterometer design. The received signal is corrupted by additive noise. Thus, in order to determine the backscattering-only contribution to the total power and to increase the measurement accuracy, the scatterometer performs a measure of the noise only signal. C-band scatterometers measuring the noise work as microwave radiometers. The power of that noise signal is subtracted from the echo+noise-signal power measurement in order to get the echo-only power signal

$$P_s = P_{s+n} - P_n \tag{1}$$

where P_{s+n} is the signal+noise power, P_n is the noise power and P_s is the signal only power.

In this paper the scatterometer noise signal P_n is analyzed. In fact, the scatterometer noise signal is a superposition of two components, the instrument noise (receiver thermal noise) and an external noise collected by the antenna (Earth radiance). The two components add in power or in noise temperature as

$$P_n = P_{nr} + P_{na} = KB(T_r + T_a) \tag{2}$$

Where P_n is the measured noise power, K is the Boltzmann constant, T_r and T_a are the receiver and the antenna noise temperatures respectively and B is the receiver bandwidth for the noise measurement. In this paper, the analysis is based on the C-band fan-beam scatteromters processing scheme. The results shown along this paper are from ERS-2/AMI and Metop-A/ASCAT data. Since ERS-1/AMI and ERS-2/AMI (and similarly Metop-A/ASCAT and Metop-B/ASCAT) are identical radars and processors, the analysis applies to all these scatterometers.

AMI and ASCAT are both real aperture C-band side looking radars using fixed fan-beam vertically polarized antennas. AMI uses three antennas called fore, mid and aft separated by 45 degrees in azimuth. The mid beam is looking in across-track direction. ASCAT has the same configuration with an additional swath (three other antennas) looking to the left side. In addition, ASCAT swath is shifted by about 8 degrees away from the nadir compared to AMI swath.

The receiver noise temperature depends on the receiver noise figure (NF) which is usually higher or equal than 3 dB. Hence T_r is usually higher ($\geq$300 K) than the antenna noise temperature ($T_A \leq$300 K). However, along the orbit, the receiver noise temperature is assumed to be constant (independent of target) and the antenna noise temperature varies depending on the viewed target. This variation is detected in the scatterometer noise signal.

2. NOISE PROCESSING OVERVIEW

For ERS scatterometers,[1,2] 32 short pulses are transmitted each antenna cycle (fore-mid-aft) and the noise is measured on 28 pulses out of the 32. The noise signal is measured in a 1.03 ms echo-free time window, filtered and sampled at 30 kHz rate which yields 32 samples in each window. Additionally, the 28 along-track pulses of measured noise signal are averaged together. In total, $32 \times 28 = 896$ samples are averaged in the on-board processing.[2–4] The 896 noise samples in form of I and Q are squared by the on-board instrument and telemetered to the ground. On-ground, the I^2 and Q^2 averages are added to derive the noise power estimate. Furthermore, 21 along-track noise power samples are averaged by the ground-processor using a Gaussian weighting function.[3] The final averaged noise power is subtracted from the received signal+noise power.

For Metop scatterometers,[5,6] one long pulse is transmitted each antenna cycle. The noise signal is measured in a 1.24 ms echo-free time window, filtered and sampled at 412.5 kHz rate which yields 512 samples in each window. First, the noise samples are windowed using a Tukey window and then the power spectrum density is estimated. Furthermore, the power spectral densities of 40 antenna cycles are averaged along-track. The resulting noise power spectrum is transmitted to the ground. On-ground, the noise power spectrum is corrected by the receiver filter shape which is also estimated from the noise signal as is explained later. The noise power spectrum is averaged in range over a selected frequencies to derive the average noise power.[7] Finally, the average noise power is used to correct (noise subtraction) the echo power signal.

3. NOISE SIGNAL CHARACTERIZATION

3.1. Spatial distribution

Figure 1 illustrates the spatial distribution of the averaged noise power signal on a global geographic map. The first map (left) was constructed using one cycle (35 days) of ERS-2/AMI data during its regional mission scenario, hence the limited coverage. The second map (right) was constructed using six days of ASCAT data. The two maps show a clear distinction between sea, land and ice. Moreover, additional features can be distinguished on the second map. For instance, one can distinguish between cold polar and warm tropical oceans. By visual comparison of the two maps, it is apparent that ASCAT provides higher radiometric resolution than AMI. The scatterometer measures the Earth radiance R_λ. Neglecting the sky radiance and the atmospheric attenuation, in C-band frequencies, using the Rayleigh-Jeans approximation the radiance is given by

$$R_\lambda = \frac{2kT_b}{\lambda^2}. \tag{3}$$

where T_b is the brightness temperature and is related to the physical temperature by the emissivity ($T_b = eT_{phys}$).

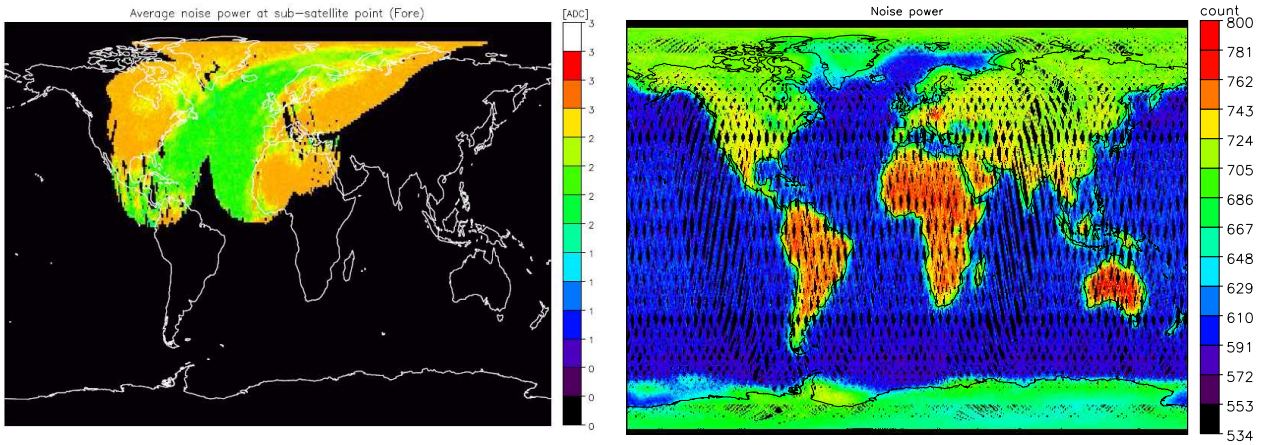

Figure 1. left: AMI noise power map - Cycle 142 18-NOV-2008 to 22-DEC-2008, right: ASCAT noise power map - 01-06 Jan 2011

3.2. Spatial resolution

In this section, we examine the spatial resolution of the noise power signal. The noise power signal is the result of the convolution of the radar antenna pattern with the brightness temperature of the surface integrated over the bandwidth of the receiver. Moreover, in the nominal products the signal is convolved with a Hamming window. The spatial resolution is examined using land-sea transition (coastline). At the coastlines, a contrast in radiance can be expected. This thus provides the step function of the observing system, from which the resolution can be deduced.

Unlike the scanning pencil beam scatterometers (e.g., SeaWinds)[8] and radiometers (e.g., AMSR-E)[9] which have small footprints, ASCAT and AMI are fixed fan-beam radars. They have large antenna footprints in range ($\approx$ 500 km) and narrow footprints in azimuth ($\approx$ 30 km). Note, that for instance AMSR-E radiometer provides a spatial resolution of 74×43 km and SeaWinds antenna footprint is approximately 37×52 km.

For the noise power measurements, the noise signal is not range gated along-the-beam. The Point Spread Function (PSF) is dominated by the antenna gain pattern and is orientation dependent. Figure 2 shows the along-track Noise Equivalent Sigma Zero (NESZ, see section 4) crossing a coastline. The orientation of the antennas footprint is illustrated with the black ellipses. The mid antenna footprint is parallel to the coast line, hence the relatively sharp transition as shown in figure 2 (red line). This is because, in this case, the noise signal has a resolution comparable to σ_0 i.e., the azimuth footprint width. On the other hand, the fore antenna footprint makes an angle of 45^o w.r.t to the coastline. Hence, it provides a smooth transition due the larger PSF in that direction.

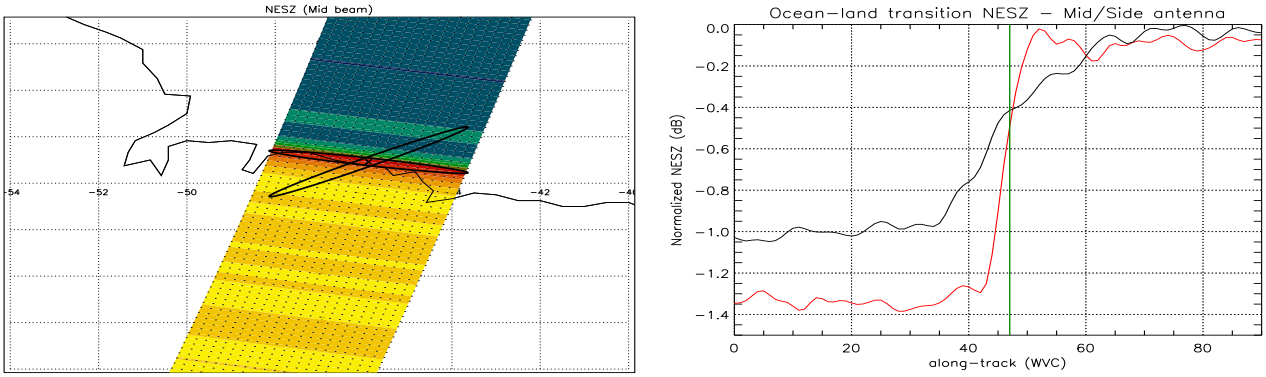

Figure 2. NESZ land-sea transition, red: Mid antenna, black: Fore antenna

3.3. Comparison with a radiometer

In this section, the ASCAT scatterometer thermal noise power measurements are compared to the Advanced Microwave Scanning Radiometer for the Earth Observing System (AMSR-E) brightness temperature.[9] The channel operating at 6.9 GHz and VV polarization is used.

First, the brightness temperature extracted from AMSR-E's products was mapped to the same grid as ASCAT. Second, a pixel-by-pixel comparison was carried out between ASCAT noise power and AMSR-E brightness temperature. Figure 3 shows the scatter plot of the two datasets. The comparison yields a very good correlation between the two datasets ($\rho \approx \mathbf{0.9}$) as is illustrated in the figure. Moreover, the scatter plot shows discernible clusters. One can easily identify ocean, sea ice, land ice and dry land with increasing T_b. Finally, After the above mentioned observations one can conclude that the noise signal measured by the scatterometer during the noise only measurement window can easily detect the thermal radiation of the observed target, which is proportional to the brightness temperature. As mentioned before, the scatterometer behaves as a low resolution radiometer in its noise only measurement window.

4. NOISE EQUIVALENT SIGMA ZERO

The accuracy of the noise subtraction algorithm is particularly important for estimating σ_0 when the SNR is low which is the case over the ocean at low wind speeds. Thus, it is possible to compute a negative σ_0 when the noise power is higher

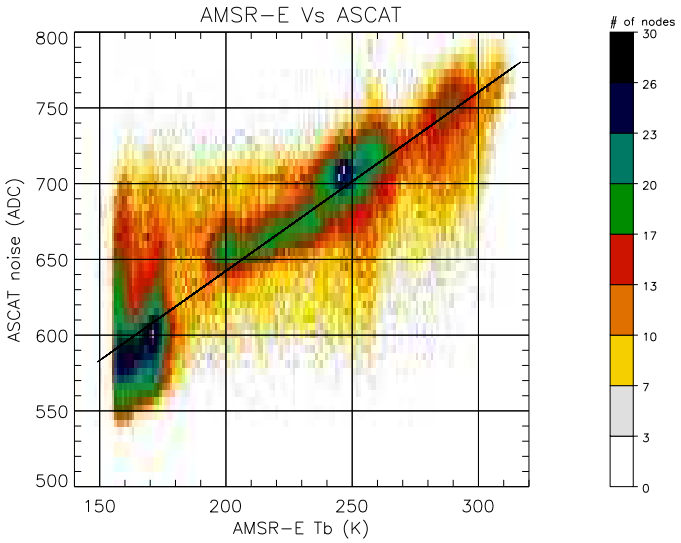

Figure 3. ASCAT noise power Vs AMSR-E brightness temperature scatter plot

than echo power. The Noise Equivalent Sigma Zero (NESZ) provides a measure of the sensitivity of the radar. A lower NESZ is better. Practically, the *NESZ* is obtained by injecting the received noise power signal into the scatterometer processor. Here, the NESZ is computed for ERS-2/AMI and Metop/ASCAT nominal resolution products (25 km grid spacing). These products are organized in rows of 19 and 21 across-track Wind Vector Cells (WVC) for AMI and ASCAT respectively. Finally, AMI NESZ and ASCAT NESZ over the ocean are shown in figure 4. The trend of the curves across the swath is due to the antenna gain pattern. The figure indicates that ASCAT has lower NESZ (higher sensitivity) than AMI e.g., at 40^o incidence angle, the difference is approximately 1 dB.

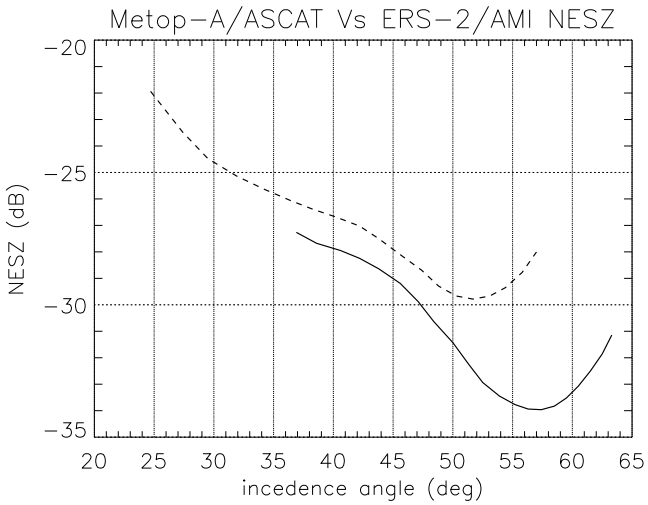

Figure 4. ASCAT and AMI NESZ, solid line: ASCAT, dashed line: AMI

5. IMPACT OF THE NOISE SUBTRACTION ON THE PROCESSING

It is essential to remove the contribution of the noise power to the received echo power prior to wind retrieval. The impact of the noise removal (subtraction) on σ_0, wind speed and the standard deviation is discussed in the following sections.

5.1. Impact on sigma naught and wind speed

In this section, the objective is to evaluate quantitatively the bias in σ_0 if no noise subtraction was performed. Figure 5 illustrates the effect of noise subtraction on the measured backscatter as a function of incidence angle (across-swath). The effect is more important toward higher incidence angles i.e. lower backscatter. The difference between the σ_0 computed with noise subtraction and the σ_0 computed without noise subtraction ranges from 0.15 dB at near swath to 1.4 dB at far swath. This is an important difference compared to the scatterometer targeted accuracy (0.2 dB). This difference can be even more important at lower backscatter values than the values found in this test dataset. This confirms as expected the necessity and importance of noise subtraction operation.

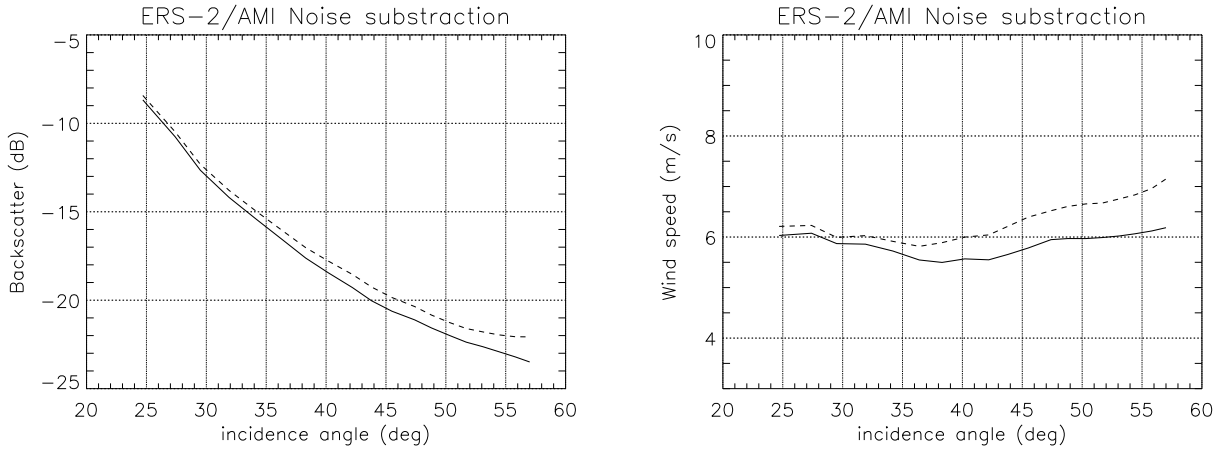

Figure 5. AMI Noise subtraction effect on backscatter (left) and wind speed (right), solid line: with noise subtraction, dashed line: without noise subtraction

The variation (increase) of the effect of noise subtraction on the backscatter in range is reflected in the wind speed as shown in figure 5 (right). The wind speed difference due to noise subtraction varies approximately between 0.2 m/s at near range to 1 m/s at far range. Again, this is a consequent bias.

5.2. Impact on the standard deviation

A metric widely used in scatterometery to characterize the σ_0 accuracy is the relative standard deviation which is called K_p. It is also an important parameter as it is used for wind retrieval. K_p is defined as the standard deviation of the echo-only signal power normalized by its power average.

$$K_p = \frac{\sqrt{var[P_s]}}{E[P_s]} \tag{4}$$

In order to evaluate the effect of noise subtraction, K_p is computed with σ_0 reprocessed with and without noise subtraction. This effect is illustrated in figure 6. As expected, noise subtraction increases K_p for both ERS-2 and Metop-A scatterometers. This is because the variance of the noise power P_n adds to the variance of the signal+noise power P_{s+n} as

$$var[P_{s+n} - P_n] = var[P_{s+n}] + var[P_n] \tag{5}$$

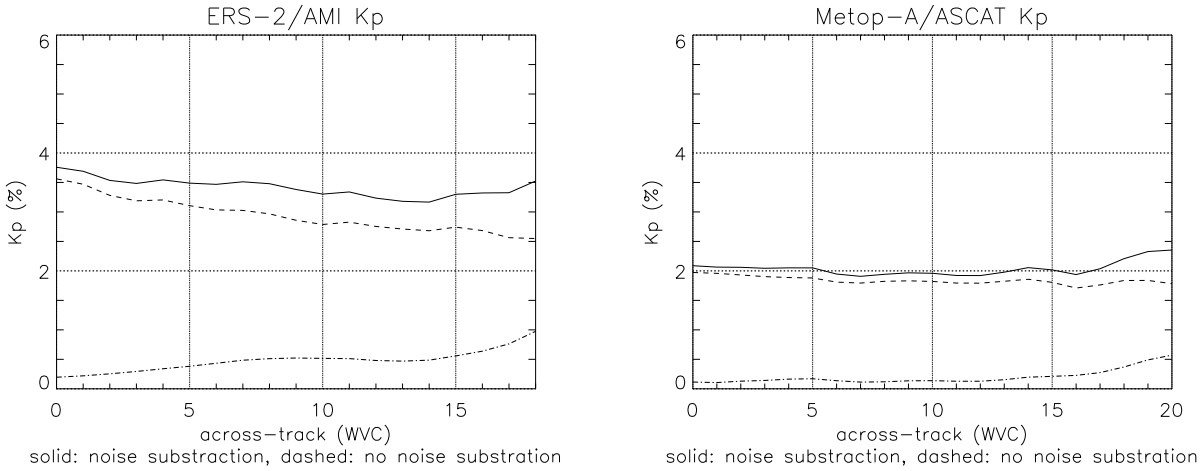

Figure 6. Noise subtraction effect on K_p; left: AMI, right: ASCAT; solid line: with noise subtraction, dashed line: without noise subtraction, dash dot line: difference

As was noticed for backscatter and wind speed, the noise subtraction have a greater effect on the lower backscatter values i.e., values near to the noise floor. For AMI, the difference in K_p varies between 0.25 % and 1 %. For ASCAT, the difference varies between 0.45 % at near range and 1.25 % at far range. This is the price to pay for noise subtraction and is inevitable.

5.3. Rx filter estimation

In ASCAT processor, the noise power spectral density is estimated on-board. The estimated noise spectrum is used to estimate the on-board receiver filter shape. The noise is assumed to be white in the 200 kHz band of the receiver filter and stationary along a portion of the orbit. This is done by averaging noise power spectra along-track and normalizing by the central bin amplitude ($f_c = 103$ kHz). A normalized filter shape is obtained as shown in figure 7. Note that only samples between 32 kHz and 192.8 kHz are considered.

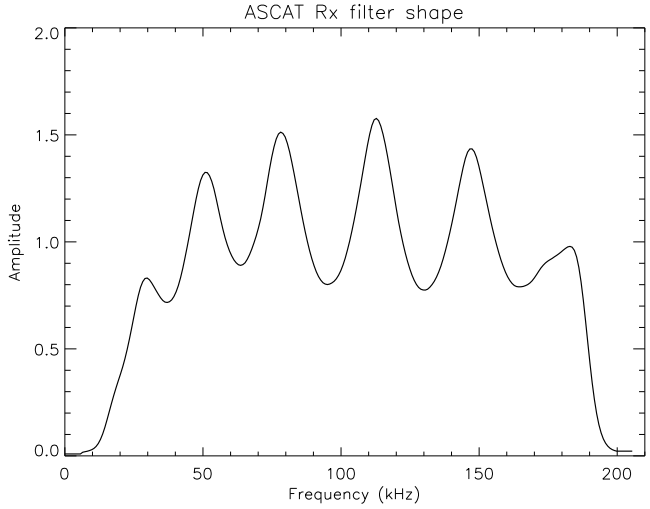

Figure 7. ASCAT receiver filter shape

The noise power depends on the viewed surface properties which might change. The noise signal variation shown earlier can have an impact on the filter processing. Actually, it was found that the receiver filter shape varies with time and space[10] and this variation is not random. Therefore, the variation of the noise power along the orbit could explain the variation of the estimated filter shape. Moreover, the estimated filter h_{rx} is used to correct the received echo power spectrum P_{s+n} (signal+noise) for the filter ripples (before noise subtraction) as follows[7]

$$P_c(f) = P_{s+n}(f)/h_{rx}(f) - P_n \tag{6}$$

where P_c is the corrected power, P_{s+n} is the received power and h_{rx} is the filter amplitude. P_n is the estimated noise power, which is also corrected for the filter ripples and averaged over a given frequency range. Therefore, variation of the filter can affect directly the power and consequently the σ_0. This needs further investigation to evaluate the exact impact of the filter variation on σ_0.

6. EFFECT OF THE VIEWING GEOMETRY

The scatterometer noise signal (Earth radiance component) is weighted by the antenna radiation pattern and amplified by the receiver gain as follows

$$T_a = G_r \frac{\int\int G(\theta,\phi) T_b(\theta,\phi) d\theta d\phi}{\int\int G(\theta,\phi) d\theta d\phi} \tag{7}$$

Where T_a and T_b are the antenna noise temperature and the target brightness temperature respectively and G_r is the receiver gain.

For the receiver gain effect one can refer to the ESA scatterometer cyclic reports to see the impact of increasing the receiver gain (e.g., on 28th February 2003) on the noise power. From the monitoring of ERS-2 scatterometer noise power, it was observed that the noise measured by the side and mid antennas differ, particularly, the mid beam noise level is much lower than the side beams.[2] Actually, the noise level in the mid beam is under one count (1 ADC), so it is set to 0. For ASCAT, the noise power measured by the mid beam is also lower (though not much lower) than side beams over ocean, while over land no clear difference is noticed (see figure 8).

In spaceborne remote sensing the observed area is larger than the antenna main beam. Thus, it can be assumed that the solid angle of the source is large enough to fill all the antenna lobes. In addition, this area can be assumed thermally uniform i.e., T_b constant over the antenna footprint. Thus, though the three antennas have different radiation patterns, they should measure the same T_b. Therefore, the difference in noise power is not likely to be due to the antenna gain pattern. If the difference between antennas noise temperature was due to the receiver gain difference it would exhibit the same offset over all type of surfaces (e.g., ocean and land). Therefore, the difference in noise power is not likely to be due to the receiver gain.

The brightness temperature T_b depends on emissivity e and physical temperature T. The emissivity depends on the relative permittivity ε_r and on the incidence angle θ. For vertical polarization the emissivity $e(\theta)$ is expressed (assuming a specular surface) as[11]

$$e(\theta) = 1 - \left| \frac{\varepsilon_r cos(\theta) - \sqrt{\varepsilon_r - sin(\theta)^2}}{\varepsilon_r cos(\theta) + \sqrt{\varepsilon_r - sin(\theta)^2}} \right|^2 \tag{8}$$

Figure 8 shows that the emissivity varies with incidence angle. The emissivity has been simulated with typical dielectric constants $\varepsilon = 80$ and $\varepsilon = 10$ for sea and land respectively. Moreover, the figure also indicates that the emissivity of water exhibits the highest angular dependence while that of land shows a lower angular dependence at the scatterometer incidence angle range. This makes the difference more apparent over sea than over land. For both scatterometers, mid antennas illuminate the swath with lower incidence angle range than side antennas. The vertical lines show approximately the mean incidence angle for the mid and side beams. Therefore, the difference of the noise level between the side and mid antennas is more likely to be due to incidence angle difference.

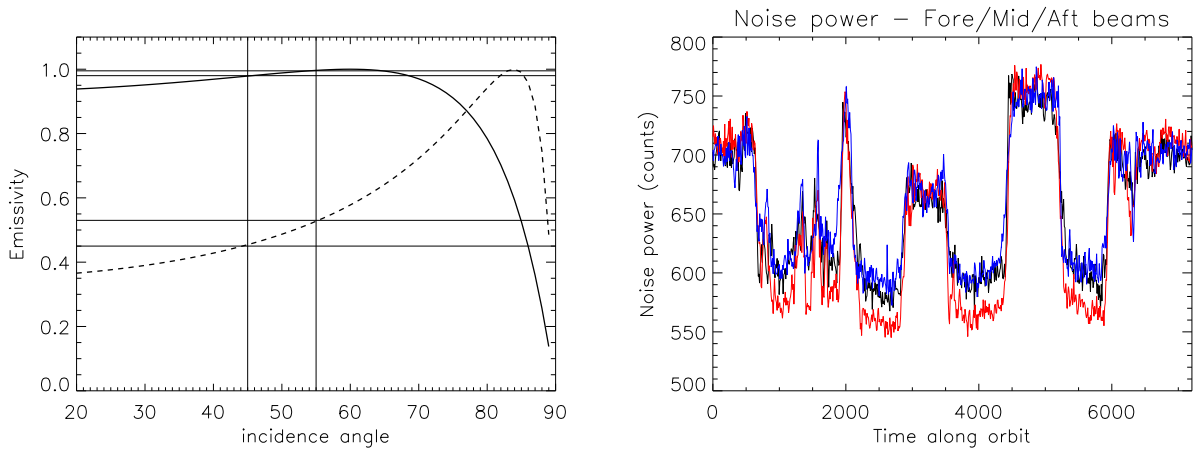

Figure 8. Emissivity (left), solid: land, dashed: sea water; ASCAT noise power for the three beams (right), Black: Fore, Red: Mid, Blue: Aft

7. ALONG-TRACK AVERAGING EFFECT ON NOISE SUBTRACTION

In order to reduce the variance, both AMI and ASCAT processors average the echo power and the noise power over a number of pulses which corresponds to a certain along-track distance. This distance is different for the echo power and for the noise power. In this section, a possible noise power misestimation due this difference, which would induce a σ_0 bias via noise subtraction, is investigated. In ASCAT on-board processing the noise signal is averaged over 40 pulses while the σ_0 is averaged over 8 pulses spaced by 1.4 km along-track distance. This is equivalent to a ground distance of $8 \times 1.4 = 11.2$ km and $40 \times 1.4 = 56$ km for σ_0 and noise respectively. In AMI processing the noise signal is averaged on-ground over 21 along-track pulses spaced by 6.25 km. This is equivalent to a ground distance of $40 \times 6.25 = 131.25$ km. ASCAT performs box averaging for the noise and weighted averaging for σ_0 while AMI uses a Gaussian weighting function centered on the considered WVC. Averaging P_{s+n} and P_n using different filters and over different distances might induce an error in coastal WVCs where a high contrast in NESZ has been observed (see section 3.2). The impact of under/over subtraction of noise on coastal σ_0 can be estimated as the difference between an ideal subtraction and a biased subtraction. Where the ideal subtraction is when the same averaging is performed for P_{s+n} and P_n.

This gives for ASCAT

$$\begin{aligned} \sigma_{0_{dB}}^{error} &= h(t) * [[P_{s+n}(t) * w_8(t) - P_n(t) * w_8(t)] - [P_{s+n}(t) * w_8(t) - P_n(t) * w_{40}(t)]] \\ &= h(t) * [P_n(t) * w_{40}(t) - P_n(t) * w_8(t)] \\ &= h(t) * [P_n(t) * (w_{40}(t) - w_8(t))] \end{aligned}$$

For AMI

$$\begin{aligned} \sigma_{0_{dB}}^{error} &= h(t) * [[P_{s+n}(t) - P_n(t)] - [P_{s+n}(t) - P_n(t) * g_{21}(t)]] \\ &= h(t) * [P_n(t) * g_{21}(t) - P_n(t)] \end{aligned}$$

Where $P_{s+n}(t)$ is the signal+noise, $P_n(t)$ is the noise only signal, $w_8(t)$ is an 8-point trapezoidal weighting window, $w_{40}(t)$ is a 40-point rectangular weighting window, $g_{21}(t)$ is a 21-point Gaussian window. The 8-point trapezoid window weights are:[0.05, 0.10, 0.15, 0.20, 0.20, 0.15, 0.10, 0.05]. $h(t)$ is the Hamming window used in the spatial filtering of the final product and $*$ stands for convolution. $h(t)$ width is ≈ 86 km and ≈ 43 km for nominal and high resolution products. For the full resolution products (no spatial filtering), the $h(t)$ is a delta function. $P_n(t)$ is modeled as a step function of amplitude 1dB which corresponds to the contrast between land and sea (see section 3.2).

For ASCAT, it is found that only the WVCs that are closer than ≈ 30 km to the coast will be affected by the actual noise power averaging. This is equivalent to 5, 2 and 1 along-track samples in the full resolution (5.6 km), high resolution

(12.5 km) and nominal resolution (25 km) products respectively. For the affected samples, the maximum bias is 0.21 dB and 0.086 dB for high and nominal resolution products respectively as shown in figure 9. For AMI, it is found that the WVCs that are closer than ≈ 70 km to the coast will be affected by the actual noise power averaging. This is equivalent to 11, 6 and 3 along-track samples in the full resolution (6.25 km), high resolution (12.5 km) and nominal resolution (25 km) products respectively. For these affected samples, the maximum bias is 0.25 dB and 0.13 dB for high and nominal resolution products respectively. The maximum bias is roughly similar for both sensors, but the extent of the affected WVCs is larger for AMI. Finally, note that the closest WVC to the coastline is usually discarded in scatterometery studies due to land contamination of σ_0.

To summarize, the error on σ_0 due to possible noise mis-estimation and subtraction is probably negligible (≤ 0.1 dB) for nominal resolution products. While for the high resolution products the coastal WVCs must be considered with care. Finally, on one hand, reducing the along-track averaging distance of the noise power would increase its variance. On the other hand, averaging the noise power over longer distances than σ_0 affects some coastal WVCs. Thus, there is a trade-off between reducing the variance and preserving the coastal WVCs uncontaminated.

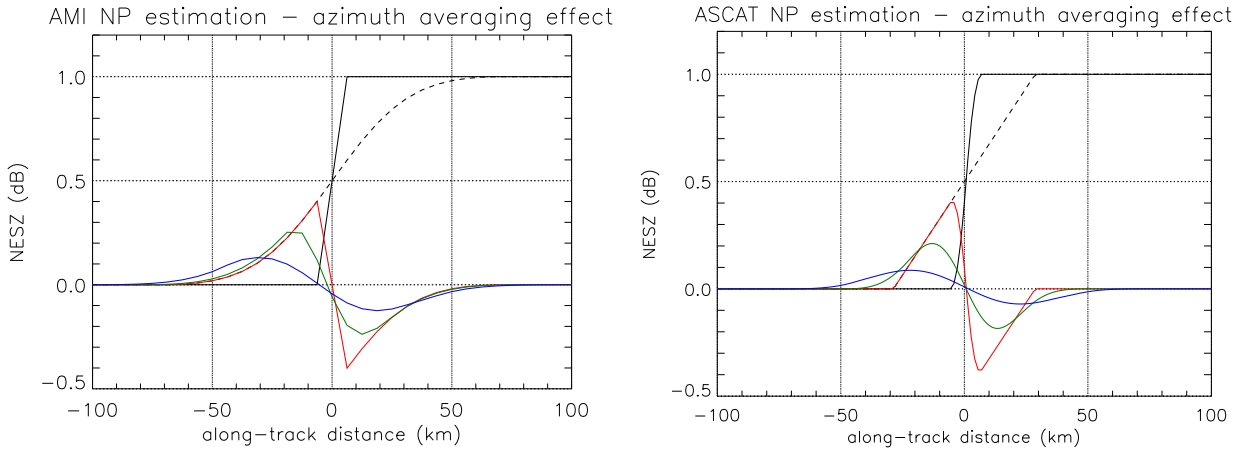

Figure 9. Along-track averaging effect on noise power; Left: black solid: P_n, black dashed: $P_n * g_{21}$, red: $(P_n * g_{21}) - P_n$, green: $h_{43} * (P_n * g_{21} - P_n)$, blue: $h_{86} * (P_n * g_{21} - P_n)$; Right: black solid: $P_n * w_8$, black dashed: $P_n * w_{40}$, red: $(P_n * w_{40}) - (P_n * w_8)$, green: $h_{43} * [(P_n * w_{40}) - (P_n * w_8)]$, blue: $h_{86} * [(P_n * w_{40}) - (P_n * w_8)]$; where h_{43} and h_{86} are the 43 km and 86 km width Hamming window and $*$ denotes convolution

8. CONCLUSION

In this paper the noise signal measured by the C-band scatterometers on-board ERS-2 and Metop-A satellites was analyzed. This analysis shows that the noise signal carries a valuable geophysical information. The temporal and spatial variation of the Earth radiance can be resolved by the scatterometer. Moreover, it was shown that this signal is proportional to the brightness temperature provided by the microwave radiometer (AMSR-E). However, the spatial resolution of the noise signal limits its usability. The noise power measured by different antennas were compared which suggested a geometry effect, mainly due to incidence angle difference. The NESZ was computed for both AMI and ASCAT and compared. The comparison led to the conclusion that ASCAT has a lower NESZ than AMI, hence a higher radiometric resolution. Furthermore, the effect of a possible under/over subtraction due to along-track averaging of the noise power near the coast was investigated using land-sea transitions. It was found that the error in coastal σ_0 is probably negligible for nominal resolution products but can be considerable for higher resolution products.

9. ACKNOWLEDGMENT

Data was provided by ESA, Eumetsat and we would like to thank these institutes. This work would not have been possible without the help of Craig Anderson (EUMETSAT) and Julian Wilson (EUMETSAT).

REFERENCES

1. Evert P.W. Attema. The active microwave instrument on-board the ERS-1 satellite. In *Proceedings of the IEEE*, volume 79, pages 791–799, June 1991.
2. P. Lecomte. The ERS scatterometer instrument and the on-ground processing of its data. In *Proc. of a Joint ESA-Eumetsat Workshop on Emerging Scatterometer Applications*, pages 241–260, Noordwijk, The Netherlands, November 1998.
3. X. Neyt, P. Pettiaux, M. D. Smet, and M.Acheroy. Scatterometer algorithm review for gyro-less operation. Technical Report RMA-SIC-011109, Royal Military Academy, December 2001.
4. P. Pettiaux, X. Neyt, and M. Acheroy. Validation of the ERS-2 scatterometer ground processor upgrade. In *Proceedings of the SPIE: Remote Sensing of the Ocean, Sea Ice, and Large Water Regions, Crete, Greece*, volume 4880, September 2002.
5. J. Figa-Saldaa, J.J.W. Wilson, E. Attema, R. Gelsthorpe, M.R. Drinkwater, and A. Stoffelen. The advanced scatterometer (ASCAT) on the meteorological operational (METOP) platform: A follow on for european wind scatterometers. *Can. J. Remote Sensing*, 28(3):404412, 2002.
6. X. Neyt, N. Manise, and M. Acheroy. Analysis of the impact of ASCAT's pulse compression. In *Proceedings of the SPIE: Remote Sensing of the Ocean, Sea Ice, and Large Water Regions*, volume 6360, September 2006.
7. J. Wilson and J. Figa-Saldana. ASCAT product generation function specification. Technical Report EUM.EPS.SYS.SPE.990009, EUMETSAT, Darmstadt, 2002.
8. M. W. Spencer C. Wu and David G. Long. Tradeoffs in the design of a spaceborne scanning pencil beam scatterometer: Application to Seawinds. *IEEE Transactions on Geoscience and Remote Sensing*, 35(1):115–126, January 1997.
9. T. Kawanishi, T. Sezai, Y. Ito, K. Imaoka, T. Takeshima, Y. Ishido, A. Shibata, M. Miura, H. Inahata, and R. W. Spencer. The advanced microwave scanning radiometer for the earth observing system (AMSR-E), nasda's contribution to the EOS for global energy and water cycle studies. *IEEE Transactions on Geoscience and Remote Sensing*, 41(2):184–194, February 2003.
10. J. Figa-Saldana and C. Anderson. ASCAT-B level 1 commissioning report. Technical Report EUM/OPS/DOC/12/3436, EUMETSAT, Darmstadt, 2013.
11. F. T. Ulaby, R. K. Moore, and A. K. Fung. *Microwave remote sensing : active and passive. 2. , Radar remote sensing and surface scattering and emission theory*. Remote senging. Artech house, London, 1986.